Axial compressive behavior and energy absorption of syntactic foam-filled GFRP tubes with lattice frame reinforcement

Qing Jin [a], Jun Wang[a,] *, Jiye Chen[b], Fengling Bao[c]

[a]College of Civil Engineering, Nanjing Tech University, Nanjing, People's Republic of China

[b]School of Civil Engineering and Surveying, University of Portsmouth, UK

[c]Nanjing Urban Construction Management Group Co. Ltd, People's Republic of China

Abstract: A kind of innovative foam-filled glass fiber-reinforced polymer (GFRP) tube with lattice frame reinforcement was proposed for improving energy absorption capacity. The crushing experimental results revealed that lattice frame reinforcement contributed to increasing compressive strength and energy absorption, by ~33 and 90%, respectively, for syntactic foam-filled GFRP tubes and their plateau stress almost increased to peak strength. Decreasing distances between transverse or vertical bars resulted in increasing energy absorption in composite columns with GFRP shells. The effects of lattice frames on the mechanical behaviors of composite columns without GFRP shells was less significant compared to columns with shells. Under the same content in foam cores, the energy absorption ability of syntactic foam-filled GFRP tubes with lattice frame reinforcement was much higher than that of specimens reinforced by MWCNTs. In addition, an analytical model considering the local buckling of lattice frames was proposed to predict the ultimate crushing load of composite columns with reinforcement. The analytical solutions agreed well with experimental results. This study provided a promising approach for designing a lightweight composite column with a high capacity for energy absorption, which could be used as an energy absorption member in engineering structures.

Corresponding author. E-mail address: wangjun3312@njtech.edu.cn (J. Wang).

Keywords: Lattice frame; GFRP tube; Syntactic foam; Axial compressive behavior; Energy absorption

1. Introduction

Thin-walled fiber-reinforced polymer (FRP) tubular components have been applied widely in crash-absorption structures because of their facile fabrication, adjustability, and high energy absorption ability [1, 2]. However, FRP tubes usually exhibit brittle failure mechanisms due to the brittle nature of the fibers (e.g., glass, carbon, or aramid fibers). Lightweight foams have been increasingly applied as a core material of FRP tubes to enhance impact resistance, buckling strength, and stiffness while maintaining minimal mass [3, 4]. Syntactic foam composites, synthesized by incorporating hollow glass microspheres (HGMs) in a polymer matrix, have emerged as an attractive core material for sandwich structures due to their high compressive strength and specific energy absorption, low moisture absorption, and excellent damage tolerances [5-7]. FRP tubes with syntactic foam cores are expected to provide better energy absorption ability and improve buckling strength, compared to traditional porous foams.

The most common lightweight filler materials proposed in the literature include polymeric foams, such as polyisocyanurate and polyurethane foams [8, 9], timber [10], metallic foams, such as aluminum (Al) foam [11, 12], and syntactic foams [13]. Tomlinson and Fam [8] have revealed that the filling of polyisocyanurate foam contributes to prevent premature failure of outer flax fiber-reinforced polymer (FFRP)

tubes. To achieve similar structural properties, an FFRP tube should be ~1.8 times thicker than the glass fiber-reinforced polymer (GFRP) tube [8]. Wang et al. [9] have reported that polyurethane foam-filled GFRP tubes have 190% higher compressive strength and 1050% higher energy absorption compared to Al-fly ash syntactic foam-filled Al tubes. Zhang et al. [14] have confirmed that polyurethane foam is a better choice than Al foam for improving specific energy absorption (SEA, energy absorption per unit mass) of GFRP tubes. Chen et al. [15] have conducted axial compression tests on the slender GFRP-polyurethane foam composite columns with a slenderness ratio from 27/1 to 90/1. Overall buckling dominates the failure mode of these slender columns under compression and the polyurethane foam core in the linear elastic stage during the tube buckling process [15]. Sun et al. [16] have reported that the SEA of carbon fiber-reinforced polymer (CFRP) tubes filled with higher density Al foams (0.45 g/cm^3) is lower than that of CFRP tubes filled with lower density Al foams (0.23 and 0.32 g/cm^3). This was due to circumferential and axial cracks occurring at the CFRP tube wall. GFRP tubes exhibit better crashworthiness than CFRP tubes under low velocity impact and, thus, GFRP preferable for designing thin-walled structures for low velocity impact resistance [3]. Syntactic foams are closed-cell composite foams, which provide excellent mechanical properties compared to open-cell foams. Granular materials can partially dissipate applied energy trapped as elastic energy in stretchable components and partially dissipate energy through friction between microspheres [17]. The matrix of syntactic foam can be selected from polymer, metal, ceramic material. Epoxy resin have shown many advantages such as good adhesion to particles, low

shrinkage on curing, corrosion resistance, high strength, and excellent dimensional stability, which are important for the industry applications [18,19]. The fillers of syntactic foam can be hollow ceramic, glass, carbon, polymer and metal microspheres, in which hollow glass microsphere (HGM) is one of the commonly used hollow particles for its lightweight, cost effective and relatively high strength [20,21]. The mechanical properties of syntactic foam are significantly affected by the constituents of the foams. Syntactic foams with smaller particulates or higher wall thickness-to-diameter ratio have a high compressive strength and density [22]. Swetha and Kumar [23] have reported that with increase in the content of microspheres, the energy absorption capacity of the HGMs/epoxy resin syntactic foam increases till a critical volume fraction and then decreases. The compressive test results of Huang and Li [24] have revealed that micro-cracks in the epoxy resin matrix tend to propagate to join adjacent micro-cracks and voids left by fractured microspheres, and finally develop into a macro-crack either in the preferred vertical (for volume fraction of microspheres no more than 0.2) or diagonal (for volume fraction of microspheres more than 0.3) directions.

Syntactic foam is considered to be one of the most promising core materials for sandwich construction [25, 26]. Several studies have been conducted to better understand the mechanical behavior of the combination of FRP and syntactic foam. Qi et al. [27] have investigated the bonding performance between syntactic form cores and CFRP skins and examined the flexural properties of sandwich composites with thermoplastic and thermoset syntactic foam cores. Both thermoplastic and thermoset

syntactic foams exhibit good adhesive properties with CFRP face-sheets. The flexural strength of sandwich composites with epoxy-matrix syntactic foam cores is 33% higher than that of sandwich composites with polypropylene (PP)-matrix syntactic foam cores [27]. The experimental results of Omar et al. [28] have confirmed the reinforcing effects of CFRP face-sheets on syntactic foam sandwich composites under quasi-static conditions (strain rate of 10^{-3} s^{-1}), whereas this reinforcing effect diminishes under high strain rate conditions (525 - 845 s^{-1}). This is because failure modes of the specimens change from ductile to brittle when loading conditions vary from quasi-static to high-strain rate compression. Breunig et al. [29] have reported that CFRP-syntactic foam composite panels with 60% cenosphere volume fraction experienced localized compression/crushing at applied impact energies of 80 and 160 J, whereas specimens with 20 and 40% cenosphere volume fraction experiences shear cracking and core/face-sheet debonding at these impact energies. Ahmadi et al. [30] have investigated high-velocity impact responses of syntactic foam core sandwich panels with fiber-metal laminate skins. Sandwich panels with a front Al stacking sequence supply the least residual velocity (26.9%) and most energy absorption (46.5%) in comparison with front GFRP-stacked sequences, which might be attributed to higher stiffness and strength of the Al layer. Through tuning the structural design, FRP-syntactic foam composite structures could achieve superior load carrying capacity and energy absorption.

The energy absorption ability of syntactic foams has been improved by seeking to develop stiffened or lattice core composite structures. Li and Muthyala [31] have proposed a novel integrated sandwich structure with an orthogrid-stiffened HGM/epoxy

resin syntactic foam core. The better performance of this integrated sandwich structure under impact lies in the small cell size which leads each bay toward a quasi-static impact response and thus localized and micro length-scale damage [31]. Wang et al. [32] have developed a multi-cell GFRP tube filled with HGMs/epoxy resin syntactic foam core. They concluded that increased numbers of layers of GFRP cross-shaped webs from 0 to 4 contributes to increased energy absorption of GFRP by 48%. Kumar and Ahmed [33] have reported that incorporating resin-impregnated paper honeycomb in syntactic foam contributes to increased compressive strength by 73% and energy absorption by 78% for GFRP-syntactic foam sandwich composites. Huang et al. [34] have investigated the reinforcing effects of ceramic spheres on the dynamic failure mode of composite tetrahedral truss cores under compressive loads with varying strain rates. They stated that the cluster of spheres causes node failure of the strut under impulsive loading, rather than strut buckling and fracture.

Incorporating FRP tubes or carbon nanotubes (CNTs) into the foam is another strategy for improving the bearing capacity and strength of porous foam materials. For example, Alia et al. [35] have proposed a novel tube-reinforced sandwich core structure in which chamfered CFRP tubes are embedded in crosslinked polyvinyl chloride (PVC) foams. They reported that the highest SEA value of 86 kJ/kg is achieved in multitube foams, much higher than the values in Al honeycombs and carbon fold-core structures and foams. An and Fan [36] have reported multi-CFRP tube Al foams that offer 13–30% higher compressive strength than a linear summation of the components. Embedding FRP tubes in a foam structure serves to modify the failure process occurring within the

composite tubes, greatly enhancing their energy absorption ability. FRP tube-reinforced low-density foams are suitable as energy-absorbing members [37]. The test results of Zhang et al. [38] have revealed the SEA of carbon fiber tube-reinforced polyurethane foam (CPM) filled CFRP columns to be 66% higher than that of CPM-filled aluminum columns. Esmaeili et al. [39] have stated that the maximum enhancement of tensile strength of epoxy is 28% at 0.25-wt% multiwalled carbon nanotubes (MWCNTs) and the maximum enhancement of Young's modulus by the epoxy 5.4% at 0.5-wt% MWCNTs. Wang et al. [40] have investigated the low-velocity impact responses of syntactic foams with amine-treated HGMs and acid-treated MWCNTs. Amine treatment is an effective strategy for improving the impact resistance of syntactic foams, while merely modifying MWCNTs by acid treatment has little effect on composite impact resistance [40]. CNTs aligned transversely to a crack provide a bridge for transferring load and hinder crack propagation, thus enhancing the fracture toughness of a polymeric matrix. Also, the pulling-out of CNTs from the matrix contributes to dissipate much more energy [41]. However, high amounts of CNT additives can agglomerate in the resin matrix, thus impeding full utilization of the superior mechanical properties of CNTs. As FRP cylindrical tubes or bars are widely available in the market, tubular-reinforced sandwich structures can provide considerable potential benefits, including convenient fabrication, superior energy-absorbing characteristics, and relatively low cost. Through the reasonable arrangement of embedded tubes or bars, syntactic foam composites might achieve excellent mechanical properties with little increase in cost.

The HGMs/ epoxy resin syntactic foam is attractive as an ideal core material for composite tubes because of its lightweight, easy-shaping, high strength to weight ratios and good impact resistance [42,43]. Properly designed FRP-syntactic foam composite tubular structures could achieve superior structural and energy absorption properties. In this study, a novel HGMs/epoxy resin syntactic foam-filled GFRP tubular column was proposed in which the foam core was reinforced by a GFRP lattice frame. GFRP shells and distances between GFRP bars in transverse and vertical directions were varied to examine the mechanical behavior of these composite columns under compression. Moreover, the reinforcement effects of lattice frames on the structural behaviors of composite columns were compared with those of specimens reinforced with MWCNTs. An analytical model was then developed to predict the ultimate peak strength of these tubes with lattice frame reinforcement, in which the confinement effect on these foam cores and the local buckling of GFRP shells and lattice frames were evaluated.

2. Materials and experimental programs

2.1 Materials

GFRP tubes are tubular laminated products made of E-glass fabric impregnated with epoxy resin by hot-rolled, dried, and solidification steps. The mechanical properties of GFRP tubes provided by manufacturer were compressive strength 240 MPa, compressive modulus 12 GPa, Poisson's ratio 0.3, tensile strength 280 MPa, tensile modulus 14 GPa in the axial direction, tensile strength 600 MPa, tensile modulus 22 GPa, and Poisson's ratio 0.22 given in the hoop direction. The density of GFRP was

1900 kg/m^3.

E-glass fiber and isophthalic polyester resin were used to produce GFRP bars by a pultrusion process. The mechanical properties of these GFRP bars, provided by manufacturer, were compressive strength of 260 MPa, compressive modulus of 24 GPa, tensile strength of 410 MPa, and tensile modulus of 28 GPa. The amount of fiber volume percent in GFRP tubes and bars was close to 70%.

Syntactic foams were fabricated at the State Key Laboratory of Materials-Oriented Chemical Engineering of Nanjing Tech University (Nanjing, China). Low-viscosity epoxy resin was used as the base polymeric binder with the supplied specific hardener at a 10/3 weight ratio. The epoxy resin had a nominal curing time of 24 h at 25°C. Hollow glass spheres (K25) provided by 3M Co. (St. Paul, MN, USA) were used as the filler material, in which the stated dimensions of these glass spheres were varied from 25 to 95 μm, with a mean diameter of 55 μm and a thickness of 0.95 μm. The manufacturing method of the syntactic foam followed that of Ref. [4]. This previous investigation has indicated that syntactic foam containing 70-vol% HGMs has higher energy absorption ability and lower density than syntactic foam containing 50-vol% HGMs. Therefore, the volume fraction of glass spheres in the matrix was determined to be 70% in this study.

Properties of MWCNTs provided by the manufacturer possessed outer diameters of 3–15 nm, length of 15–30 μm, bulk density of 2100 kg/m^3, Young's modulus of 900 GPa, Poisson's ratio of 0.19, and purity of 97 wt%.

2.2 Test specimens

The lattice frame was formed by GFRP bars. A silicone mold with holes of the size of GFRP bar diameter was applied to keep the vertical bars at the design locations. The height of the silicone mold was determined according to the distance between the lower transverse bars and the end of the vertical bars. Then, the transverse bars were attached to the vertical bars by epoxy adhesive at the design locations. The formed lattice frame was placed into the GFRP tube. The manufacturing procedures of syntactic foam reinforced by MWCNTs have been presented in a previous study [40]. After homogeneous dispersion raw material mixtures, the resulting syntactic foam mixtures were poured into GFRP tubes to form composite columns. The fabrication procedure of these composite columns with lattice frame reinforcement is shown in Figure 1.

Two groups of specimens were fabricated to evaluate confinement effects, including (1) syntactic foam columns without GFRP shells and (2) syntactic foam-filled GFRP tubular columns. In each group, the weight fractions of MWCNTs in the syntactic foams were 0, 0.6, and 1.2% and the lattice frames had three different types. A further increase in the weight fraction of MWCNTs might have caused agglomeration in the resin matrix. The mechanical properties of bare syntactic foam and syntactic foams reinforced with 0.6 and 1.2-wt% MWCNTs are presented in Table 1. The distance between vertical bars was varied from 12.5 to 20 mm and the distance between the transverse bars in the axial direction from 20 to 40 mm. The weight ratios of lattice frames I, II, and III to the syntactic foam were 1.1, 1.3, and 2.2%. To compare reinforcement effects of the lattice frame and MWCNTs, the first two weight ratios of

the lattice frame were set to be similar to the higher weight fraction of MWCNTs. The details of the specimens are listed in Table 2.

GFRP tubes had an inner diameter of 50 mm and wall thickness of 2 mm. All test specimens had the same height of 80 mm and the syntactic foam core diameter at 50 mm. The ratio of the inner diameter to height (D/h) of the columns was 0.625, which was close to that of CFRP and Al tubes in Ref. [44], at D/h = 0.6. The diameter of the GFRP bars was 1 mm and the dimensions of GFRP confined syntactic foam columns with three kinds of lattice frames were shown in Figure 2.

2.3 Experimental Setup

Three identical specimens were tested for each composite column. The quasi-static compressive tests of specimens were performed on a 600 kN universal testing machine. The loading speed of quasi-static testing was usually kept at a constant value in the range of 1.5 to 20 mm/min [45]. Hence, axial loads were applied at a rate of 5 mm/min. During testing, the upper steel platen of the machine moved downward to crush the columns placed on the fixed lower steel platen. The crushing load was measured with a load cell amount on the upper platen and deflections recorded using outputs from the machine. All specimens were loaded until they were completely crushed or became fully densified. The test setup and measurement system are shown in Figure 3.

3 Results and Discussion

3.1 Compressive behavior and failure mode

Load-displacement curves of a composite column without a GFRP shell showed

that test specimens without a GFRP shell exhibited a three-phase displacement, including (1) linear-elastic, (2) post-yield, and (3) foam densification phases (Fig. 4a). The loads of these columns increased to their maximum values, followed by a gradual decrease with increased displacement, and then stayed at roughly one-third or a quarter of peak strength level. The initial peak load P_{max} was defined as the first peak in the load-displacement curves. A sudden load drop after the peak load corresponded to the formation of cracks in the specimens. P_m is used to denote the average sustained load in the post-yield phase. The post-yield phase was associated with microsphere crushing, resulting in continuous energy absorption and a slight increase in load owing to the increase in density from local crushing of syntactic foam. At the end of post-yield phase, the axial shortening of the columns was very large. After that, the axial compressive load of the columns tended to rise rapidly, corresponding to the initiation of the densification stage. The load-displacement curves of syntactic foam columns with MWCNTs or with lattice frame reinforcement had a similar trend, compared to bare syntactic foam columns.

Syntactic foam-filled GFRP tubular columns without lattice frame reinforcement exhibited a four-phase displacement, including (1) linear-elastic, (2) first post-yield, (3) second post-yield, and (4) foam densification phases (Fig. 4b). As the axial load increased to peak value, initial damage at the end of the GFRP tube was triggered, leading to decreased load. Then, the load remained at 60–80% of peak strength. In the third phase, the load decreased due to compressive failure of GFRP jackets and then remained at 40–50% of peak strength. P_{m1} and P_{m2} are used to denote the average

sustained loads in the first and second post-yield phases, respectively. In these two post-yield phases (phases II and III), the microspheres were crushed, thus absorbing energy. The load-displacement curves of these columns reinforced by MWCNTs exhibited similar behavior to the above columns.

Syntactic foam-filled GFRP tubular columns with lattice frame reinforcement also exhibited a four-phase displacement (Fig. 4c). The axial load increased to peak strength and stayed at peak strength as displacement increased, which indicated excellent ductility for this kind of composite columns. In the third phase, the compressive failure of GFRP jackets led to a drop in load, which then remained at ~50% of peak strength, with microsphere crushing continuing to dissipate energy.

Examination of the progressive failure of test specimens during compression showed that, for bare syntactic foam columns, vertical cracks typically initiated at the ends of the columns (Fig. 5). Then, cracks propagated along the axis and more cracks formed. Finally, the foam column was split into several blocks. For syntactic foam columns with lattice frame reinforcement, the vertical bars were buckled with increased compressive load, followed by fracture and extrusion from the foam, which resulted in crushing of the foam. The separation of foam fragments was partially suppressed by the presence of the lattice frame. For syntactic foam-filled GFRP tubular columns without a lattice frame, structural collapse initiated at one end of the GFRP tube and delamination of GFRP shell generated, resulting in outward fronds, and then the GFRP shell torn to several strips accompanied by crushed fragments of foam core. The addition of MWCNTs in the foam did not change the failure modes of bare syntactic

foam columns and syntactic foam-filled GFRP tubular columns. The failure mode of syntactic foam-filled GFRP tubular columns with frames was characterized by progressive end crushing of the GFRP tube and fracture of the tubal shell at the mid-height of the column with the foam core extruding out of the GFRP skin. Buckling and rupture of the lattice frame was observed on the foam core.

3.2 Energy absorption parameters

The maximum peak crushing load P_{max} was defined as the first peak in the load-displacement curves. For specimens with only one post-crushing phase, the average sustained load in the post-crushing phase P_m was given by

$$P_m = \frac{1}{\delta_{st} - \delta_\mu} \int_{\delta_\mu}^{\delta_{st}} P \cdot d\delta \quad , \tag{1}$$

where P is the applied crushing load, δ the axial displacement, δ_μ the total displacement in linear-elastic phase, and δ_{st} the total displacement at the start of foam compaction phase.

For the specimens with two post-crushing phases, the average sustained loads in the first and second post-crushing phases P_{m1} and P_{m2} were given by

$$P_{m1} = \frac{1}{\delta_s - \delta_\mu} \int_{\delta_\mu}^{\delta_s} P \cdot d\delta \quad \text{and} \tag{2}$$

$$P_{m2} = \frac{1}{\delta_{st} - \delta_s} \int_{\delta_s}^{\delta_{st}} P \cdot d\delta \quad , \tag{3}$$

where δ_s is the total displacement at the start of the second post-crushing phase.

The axial stiffness K was defined as the slope of the load-displacement curve in the linear-elastic phase, as given by

$$K = \frac{P_{max}}{\delta_{\mu}} \tag{4}$$

The energy absorption capacity E was calculated from the load-displacement curves, as given by

$$E = \int_0^{\delta_{st}} P d\delta \tag{5}$$

The specific energy absorption (SEA) was defined as the energy absorption per unit mass. The crush force efficiency (CFE) was the ratio of the average sustained load P_m (or the average of P_{m1} and P_{m2} for specimens with two post-crushing phases) to peak crushing load P_{max} [32]. The energy absorption parameters are summarized in Table 2.

The influence of the lattice frame on peak crushing load P_{max} and axial stiffness in linear-elastic phase K of the syntactic foam columns (S70, S70-I, S70-II, and S70-III) are shown in Figure 6a. Lattice frame reinforcement contributed to increase P_{max} and K by 17–24% and 1–11%, respectively. The P_m of specimen S70-III was a little lower than those of specimens S70-I and S70-II, which was because the foam cover for reinforcement at the bottom end of S70-III fractured earlier than those of specimen S70-I and S70-II, leading to decreased pressed area and load carrying capacity. The axial stiffness of specimens gradually increased with decreased distances between GFRP bars in transverse or vertical directions. E and SEA increased by 34–40 and 31–38%, respectively, for syntactic foam column specimens with lattice frame-I, II, and III, compared to the counterparts without lattice frame reinforcement (Table 2). These results indicated that lattice frame reinforcement improved energy absorption in syntactic foam column specimens. The different kinds of lattice frame reinforcement had insignificant effects on specimen energy absorption ability. This might be attributed

to the fact that the spalling of the foam cover weakened frame reinforcement effects. In addition, syntactic foam column specimens with lattice frame reinforcement had a CFE ratio of 0.43 to 0.55, which was higher than in specimens without lattice frame, at 0.34.

The effects of MWCNT content on P_{max} and K of syntactic foam columns (S70, S70C0.6, and S70C1.2) showed that, when the MWCNT content increased from 0 to 0.6 and 1.2 wt%, P_{max} increased by 11 and 18% and K increased by 5 and 21%, respectively (Fig. 6b). This indicated that the addition of 1.2-wt% MWCNTs had almost the same effects on the peak crushing load and higher axial stiffness of syntactic foam columns as the lattice frame reinforcement. E increased by 16 and 32% and SEA increased by 14% and 29%, respectively, for syntactic foam column specimens with 0.6 and 1.2-wt% MWCNTs, respectively (Table 2). The energy absorption ability of syntactic foam column specimens reinforced with 1.2-wt% MWCNTs was a little lower than that of specimens with lattice frame reinforcement. In addition, the syntactic foam column specimens reinforced with MWCNTs had a CFE ratio around 0.45.

The observed effects of the lattice frame on P_{max} and K of the syntactic foam-filled GFRP tubular columns (FS70, FS70-I, FS70-II, and FS70-III) showed that lattice frame reinforcement contributed to increase P_{max} and K by 31–33 and 7–18%, respectively (Fig. 6c). Decreased distances between GFRP bars in transverse or vertical directions had more significant effects on axial stiffness than peak crushing load. E and SEA increased by 74–91 and 71–87%, respectively, for syntactic foam-filled GFRP tubular columns with lattice frame-I, II, and III, compared with counterparts without lattice frame reinforcement (Table 2). These results indicated that reinforcement remarkably

improved the energy absorption of specimens with GFRP shells. This was because specimens with shells underwent remarkable deformation before fracture and maintained their peak crushing load capacity until specimen shortening increased to 1/3–1/2 height of the columns, resulting in full utilization of the properties of the GFRP shell, syntactic foam, and lattice frame. With decreased distances between GFRP bars in transverse or vertical directions, the energy absorption of the specimens with shells increased. Moreover, syntactic foam-filled GFRP tubular columns with reinforcement had a CFE ratio of 0.97–1.03 in the first post-yield phase and 0.52–0.83 in the second post-yield phase. A high ratio of CFE was associated with progressive crushing and gradual buckling and absorbed most of the applied energy, thus minimizing impact damage [45].

Examination of the effects of MWCNT content on P_{max} and K of syntactic foam-filled GFRP tubular columns (FS70, FS70C0.6, and FS70C1.2) showed that, when the content of MWCNTs increased from 0 to 0.6 and 1.2-wt%, P_{max} increased by 26 and 32% and K increased by 3 and 50%, respectively (Fig. 6d). The addition of 1.2-wt% MWCNTs in the foam core contributed to enhancing axial stiffness in specimens with GFRP shells more significantly than did lattice frame reinforcement. E increased by 16 and 22% and SEA increased by 14 and 21%, respectively, for syntactic foam-filled GFRP tubular columns with 0.6 and 1.2-wt% MWCNTs, respectively (Table 2). The energy absorption ability of GFRP-confined specimens reinforced with MWCNTs was much lower than that of specimens with lattice frame reinforcement. In addition, GFRP-confined specimens reinforced with MWCNTs had a CFE ratio of 0.71–0.82 in the first

post-yield phase and 0.37–0.49 in the second post-yield phase. The CFE values of GFRP-confined specimens were lower than those of specimens with lattice frame reinforcement.

According to the compressive test results of Maranan et al. [46], the columns reinforced with both longitudinal and transverse GFRP bars failed in a more ductile manner than the columns with only longitudinal bars. This is because the outward buckling of longitudinal bars can be prevented by the transverse hoops. The closer spacing of the transverse GFRP bars, the less brittle the compression failure of the columns, whereas the confining effect of the transverse bars on the core disappears when the transverse bars are spaced more than half the minimum core cross section [46, 47].

3.3 Cost analysis

Material costs of the composite tubes can be obtained from the supplier of the basic materials, including HGM, epoxy resin, GFRP tube, GFRP bar and MWCNT. The material costs of syntactic foam reinforced with lattice frame I, II and III are 7%, 9% and 16% higher than that of bare syntactic foam. When the content of MWCNTs increases from 0 to 0.6 and 1.2-wt%, the material costs of syntactic foam increase by 16 and 33%, respectively. Moreover, the material costs of foam-filled GFRP tubes with lattice frame I, II and III are 4%, 5% and 7% higher than that of counterpart without lattice frame. When the content of MWCNTs increases from 0 to 0.6 and 1.2-wt%, the material costs of foam-filled GFRP tubes increase by 9 and 19%, respectively.

For both syntactic foam columns and the foam-filled GFRP tubular columns,

incorporation of MWCNT generated higher material cost of the composite columns than did lattice frame reinforcement, while the energy absorption of MWCNT-reinforced composite columns was lower than that of specimens with frame reinforcement. The proposed syntactic foam-filled GFRP tubes with GFRP lattice frame reinforcement displayed excellent SEA and cost-effective, demonstrating great potential applications as crash-absorption components in transportation and aviation sectors.

4 Prediction of axial load capacity

4.1 Confinement model for syntactic foam core

The compressive strength of syntactic foam filled in an FRP tube can be expressed as a function of lateral confining pressure, using the following relationship [48]

$$\frac{f_c^{'}}{f_c} = 1 + k_1 \frac{f_l}{f_c} \quad , \tag{6}$$

where, f_c ′and f_c are the compressive strength of syntactic foam with an FRP shell and bare syntactic foam, respectively, k_1 the confinement effectiveness coefficient, and f_l the lateral confining pressure of FRP. As mentioned in Ref. [32], k_1 was taken as 0.83 for GFRP-confined syntactic foam.

4.2 Local buckling of GFRP tubes

The critical buckling stress of GFRP tubes with a foam core was obtained based on the theory of elastic stability [9, 49], expressed as

$$f_{cr} = \sqrt{3\left(1-\nu_s^2\right)} f_{cr,0} \left[\frac{R/t_s}{12\left(1-\nu_s^2\right)\left(\lambda_{cr}/t_s\right)^2} + \frac{\left(\lambda_{cr}/t_s\right)^2}{R/t_s} + \frac{2E_c\lambda_{cr}R}{\left(3-\nu_c\right)E_{f1}t_s^2} \right] \quad , \tag{7}$$

where $f_{cr,0}$ is the critical stress of hollow circular FRP tubes obtained from Eq. 8, v_s and v_c the Poisson ratios of the FRP tube and foam core, respectively, E_c the Young's modulus of the foam core, R the FRP tube mean radius, t_s the FRP tube thickness, and λ_{cr} the buckling half wavelength.

The critical stress of hollow circular cylindrical GFRP shells was given by [50]

$$f_{cr,0} = \left(\frac{\pi^2 D_{11}}{l_1^2}\right)\left[\begin{array}{l} m^2\left(1+2\dfrac{D_{12}}{D_{11}}\beta^2+\dfrac{D_{22}}{D_{11}}\beta^4\right)+ \\ \dfrac{\gamma^2 L^4}{\pi^4 m^2 D_{11} R^2}\cdot\dfrac{A_{11}A_{22}-A_{12}^2}{A_{11}+\left(\dfrac{A_{11}A_{22}-A_{12}^2}{A_{66}}+2A_{12}\right)\beta^2+A_{22}\beta^4} \end{array}\right] \quad (8)$$

where m is the number of buckled half waves in the axial direction, l_1 the tube length, A_{ij} and D_{ij} the extensional and flexural stiffness factors of composite laminates, respectively, and the values of β, γ, and ϕ obtained using Eqs. 9, 10, and 11 [50], with

$$\beta = \frac{nl_1}{\pi R m} \quad , \quad (9)$$

where n is the number of buckled waves in the circumferential direction and

$$\gamma = 1.0 - 0.901\left(1 - e^{-\phi}\right) \quad \text{and} \quad (10)$$

$$\phi = \frac{1}{29.8}\left[\frac{R}{\left(\dfrac{D_{11}D_{22}}{A_{11}A_{22}}\right)^{1/4}}\right]^{1/2} \quad . \quad (11)$$

4.3 Buckling of GFRP lattice frame

The energy method was used to calculate the critical value of the compressive force of lattice frames. The intersection of vertical and transverse bars was assumed to be hinged. The action of the foam on the vertical bar can be replaced by equally spaced elastic supports with equal rigidity. The rigidity of the equivalent elastic supports β

represents the magnitude of the reaction of the support per unit length of the bar if the deflection is equal to unity [49].

(1) Lattice frame-I

For lattice frame-I, the deflection curve of a vertical bar with two points hinged with transverse bars under compression was taken in the form of a Fourier sine series (Fig. 7), expressed as

$$y=\sum_{i=1}^{\infty}a_{\mathrm{I}i}\sin\frac{i\pi x}{\left(l_1-2c\right)} \tag{12}$$

The strain energy of bending of a vertical bar was given by

$$\begin{aligned}\Delta U_{\mathrm{IV}1}&=\frac{EI}{2}\left[\int_0^{l_1-2c}\left(\frac{d^2y}{dx^2}\right)^2dx+2\int_{-c}^{0}\left(\frac{d^2y}{dx^2}\right)^2dx\right]\\&=\frac{\pi^4EI}{4\left(l_1-2c\right)^3}\sum_{i=1}^{\infty}i^4a_{\mathrm{I}i}^2+\frac{\pi^3EI}{\left(l_1-2c\right)^3}\sum_{i=1}^{\infty}\left[\frac{i\pi c}{2\left(l_1-2c\right)}-\frac{1}{4}\sin\frac{2i\pi c}{l_1-2c}\right]i^3a_{\mathrm{I}i}^2\\&\quad-\frac{\pi^3EI}{\left(l_1-2c\right)^3}\sum_{\substack{n,m=1\\n\neq m}}^{\infty}n^2m^2a_{\mathrm{I}n}a_{\mathrm{I}m}\left[\frac{1}{n+m}\sin\frac{\left(n+m\right)\pi c}{l_1-2c}-\frac{1}{n-m}\sin\frac{\left(n-m\right)\pi c}{l_1-2c}\right]\end{aligned}\quad,\ (13)$$

where E and I are the Young's modulus and the inertia of GFRP bars, respectively.

The energy of deformation of the elastic supports of a vertical bar was [49]

$$\begin{aligned}\Delta U_{\mathrm{IV}2}&=\frac{\beta}{2}\left(\int_0^{l_1-2c}y^2dx+2\int_{-c}^{0}y^2dx\right)\\&=\frac{\left(l_1-2c\right)\beta}{4}\sum_{i=1}^{\infty}a_{\mathrm{I}i}^2+\frac{\left(l_1-2c\right)\beta}{\pi}\sum_{i=1}^{\infty}\left[\frac{i\pi c}{2\left(l_1-2c\right)}-\frac{1}{4}\sin\frac{2i\pi c}{l_1-2c}\right]\frac{1}{i}a_{\mathrm{I}i}^2\\&\quad-\frac{\left(l_1-2c\right)\beta}{\pi}\sum_{\substack{n,m=1\\n\neq m}}^{\infty}a_{\mathrm{I}n}a_{\mathrm{I}m}\left[\frac{1}{n+m}\sin\frac{\left(n+m\right)\pi c}{l_1-2c}-\frac{1}{n-m}\sin\frac{\left(n-m\right)\pi c}{l_1-2c}\right]\end{aligned}\quad.\tag{14}$$

Similarly, the deflection curve of a transverse bar under compression was taken in the form of a Fourier sine series, expressed as

$$x=\sum_{i=1}^{\infty}b_{\mathrm{I}i}\sin\frac{i\pi y}{\left(l_2-2b\right)}\quad . \tag{15}$$

The coefficients $a_{\mathrm{I}i}$ and $b_{\mathrm{I}i}$ were the amplitudes of the consecutive sine curves. In the case of transverse and vertical bars made from the same material, there was

$$\frac{b_{\mathrm{I}i}}{a_{\mathrm{I}i}}=\frac{l_2^2}{l_1^2}\quad . \tag{16}$$

The strain energy of bending of a transverse bar was obtained as

$$\begin{aligned}\Delta U_{\mathrm{IH1}}&=\frac{EI}{2}\left[\int_0^{l_2-2\mathrm{b}}\left(\frac{d^2x}{dy^2}\right)^2dy+2\int_{-b}^{0}\left(\frac{d^2x}{dy^2}\right)^2dy\right]\\&=\frac{\pi^4EI}{4\left(l_2-2b\right)^3}\sum_{i=1}^{\infty}i^4b_{\mathrm{I}i}^2+\frac{\pi^3EI}{\left(l_2-2b\right)^3}\sum_{i=1}^{\infty}\left[\frac{i\pi b}{2\left(l_2-2b\right)}-\frac{1}{4}\sin\frac{2i\pi b}{l_2-2b}\right]i^3b_{\mathrm{I}i}^2\\&-\frac{\pi^3EI}{\left(l_2-2b\right)^3}\sum_{\substack{n,m=1\\n\neq m}}^{\infty}n^2m^2b_{\mathrm{I}n}b_{\mathrm{I}m}\left[\frac{1}{n+m}\sin\frac{\left(n+m\right)\pi b}{l_2-2b}-\frac{1}{n-m}\sin\frac{\left(n-m\right)\pi b}{l_2-2b}\right]\end{aligned}\quad . \tag{17}$$

The energy of deformation of elastic supports of a transverse bar was

$$\begin{aligned}\Delta U_{\mathrm{IH2}}&=\frac{\beta}{2}\left(\int_0^{l_2-2b}x^2dy+2\int_{-b}^{0}x^2dy\right)\\&=\frac{\left(l_2-2b\right)\beta}{4}\sum_{i=1}^{\infty}b_{\mathrm{I}i}^2+\frac{\left(l_2-2b\right)\beta}{\pi}\sum_{i=1}^{\infty}\left[\frac{i\pi b}{2\left(l_2-2b\right)}-\frac{1}{4}\sin\frac{2i\pi b}{l_2-2b}\right]\frac{1}{i}b_{\mathrm{I}i}^2\\&-\frac{\left(l_2-2b\right)\beta}{\pi}\sum_{\substack{n,m=1\\n\neq m}}^{\infty}b_{\mathrm{I}n}b_{\mathrm{I}m}\left[\frac{1}{n+m}\sin\frac{\left(n+m\right)\pi b}{l_2-2b}-\frac{1}{n-m}\sin\frac{\left(n-m\right)\pi b}{l_2-2b}\right]\end{aligned}\quad . \tag{18}$$

The displacement of a vertical bar from its initial straight form to the equilibrium curve under compression was [49]

$$\begin{aligned}\lambda_{\mathrm{I}}&=\frac{1}{2}\left[\int_0^{l_1-2c}\left(\frac{dy}{dx}\right)^2dx+2\int_{-c}^{0}\left(\frac{dy}{dx}\right)^2dx\right]\\&=\frac{\pi^2}{4\left(l_1-2c\right)}\sum_{i=1}^{\infty}a_{\mathrm{I}i}^2+\frac{\pi}{\left(l_1-2c\right)}\sum_{i=1}^{\infty}\left[\frac{i\pi c}{2\left(l_1-2c\right)}+\frac{1}{4}\sin\frac{2i\pi c}{l_1-2c}\right]\frac{1}{i}a_{\mathrm{I}i}^2\\&+\frac{nm\pi}{2\left(l_1-2c\right)}\sum_{\substack{n,m=1\\n\neq m}}^{\infty}a_{\mathrm{I}n}a_{\mathrm{I}m}\left[\frac{1}{n+m}\sin\frac{\left(n+m\right)\pi c}{l_1-2c}+\frac{1}{n-m}\sin\frac{\left(n-m\right)\pi c}{l_1-2c}\right]\end{aligned}\quad . \tag{19}$$

The work done by compressive forces was obtained as

$$\Delta T_{\mathrm{I}} = 4P_{\mathrm{I}}\lambda_1 \ , \tag{20}$$

where P_{I} is the compressive force acted on a vertical bar.

Hence, the general equation for calculating the critical stress of frame-I was

$$\Delta U_{\mathrm{I}} = 4\left(\Delta U_{\mathrm{IV1}} + \Delta U_{\mathrm{IV2}}\right) + 8\left(\Delta U_{\mathrm{IH1}} + \Delta U_{\mathrm{IH2}}\right) = \Delta T_{\mathrm{I}} \ . \tag{21}$$

Substituting Eqs. 13, 14, 17, 18, and 20 into Eq. 21 and taking all parameters a_{Ii} and b_{Ii} except a_{I1} and b_{I1}, equal to zero, the critical load of a vertical bar was obtained as

$$P_{\mathrm{Icr}} = \frac{4\left\{\left[\frac{\pi m}{4}A_1 + \frac{1}{4}A_2\right] + \left[A_1 + \frac{A_2}{\pi}\cdot\frac{1}{m}\right]\left[\frac{1}{2}A_3 - \frac{1}{4}\sin 2A_3\right]\right\} + 8\left\{\left[\frac{\pi m}{4}B_1 + \frac{1}{4}B_2\right]\frac{l_2^4}{l_1^4} + \left[B_1 + \frac{B_2}{\pi}\cdot\frac{1}{m}\right]\left[\frac{1}{2}B_3 - \frac{1}{4}\sin 2B_3\right]\frac{l_2^4}{l_1^4}\right\}}{1 + \frac{1}{m}\left[\frac{\pi}{2}A_3 + \frac{1}{4\pi}\sin 2A_3\right]} \ , \tag{22}$$

where $A_1 = \frac{\pi EI}{\left(l_1 - 2c\right)^2}m^3$, $A_2 = \frac{\left(l_1 - 2c\right)^2\beta}{\pi^2}$, $A_3 = \frac{m\pi c}{l_1 - 2c}$, $B_1 = \frac{\pi EI\left(l_1 - 2c\right)}{\left(l_2 - 2b\right)^3}m^3$, $B_2 = \frac{\left(l_2 - 2b\right)\left(l_1 - 2c\right)\beta}{\pi^2}$, $B_3 = \frac{m\pi b}{l_2 - 2b}$, and m an integer. The lowest critical load P_{Icr} might occur with m = 1, 2, 3…. .

To find the value of β at which the number of half-waves changes from m to m+1, the following equation [49] was

$$P_{\mathrm{Icr}}(m) = P_{\mathrm{Icr}}(m{+}1) \tag{23}$$

For given dimensions of bars and a given value of β, Eq. 12 was used for determining m.

Then, the critical load of the lattice frame-I was

$$P_{\text{frame-I}} = 4P_{\text{Icr}} \quad . \tag{24}$$

(2) Lattice frame-II

For lattice frame-II, the deflection curve of a vertical bar with three points symmetrically hinged with transverse bars under compression was taken in the form of a Fourier sine series (Fig. 8), expressed as

$$y = \sum_{i=1}^{\infty} a_{\text{II}i} \sin \frac{2i\pi x}{(l_1 - 2c)} \quad . \tag{25}$$

The strain energy of bending of a vertical bar was given by

$$\begin{aligned} \Delta U_{\text{IIV1}} &= \frac{EI}{2}\left[\int_0^{l_1-2c}\left(\frac{d^2y}{dx^2}\right)^2 dx + 2\int_{-c}^{0}\left(\frac{d^2y}{dx^2}\right)^2 dx\right] \\ &= \frac{4\pi^4 EI}{(l_1-2c)^3}\sum_{i=1}^{\infty} i^4 a_{\text{II}i}^2 + \frac{8\pi^3 EI}{(l_1-2c)^3}\sum_{i=1}^{\infty}\left[\frac{i\pi c}{(l_1-2c)} - \frac{1}{4}\sin\frac{4i\pi c}{l_1-2c}\right] i^3 a_{\text{II}i}^2 \\ &\quad - \frac{8\pi^3 EI}{(l_1-2c)^3}\sum_{\substack{n,m=1 \\ n\neq m}}^{\infty} n^2 m^2 a_{\text{II}n} a_{\text{II}m}\left[\frac{1}{n+m}\sin\frac{2(n+m)\pi c}{l_1-2c} - \frac{1}{n-m}\sin\frac{2(n-m)\pi c}{l_1-2c}\right] \end{aligned} \quad . \tag{26}$$

The energy of deformation of elastic supports of a vertical bar was

$$\begin{aligned} \Delta U_{\text{IIV2}} &= \frac{\beta}{2}\left(\int_0^{l_1-2c} y^2 dx + 2\int_{-c}^{0} y^2 dx\right) \\ &= \frac{(l_1-2c)\beta}{4}\sum_{i=1}^{\infty} a_{\text{II}i}^2 + \frac{(l_1-2c)\beta}{2\pi}\sum_{i=1}^{\infty}\left[\frac{i\pi c}{(l_1-2c)} - \frac{1}{4}\sin\frac{4i\pi c}{l_1-2c}\right]\frac{1}{i} a_{\text{II}i}^2 \\ &\quad - \frac{(l_1-2c)\beta}{2\pi}\sum_{\substack{n,m=1 \\ n\neq m}}^{\infty} a_{\text{II}n} a_{\text{II}m}\left[\frac{1}{n+m}\sin\frac{2(n+m)\pi c}{l_1-2c} - \frac{1}{n-m}\sin\frac{2(n-m)\pi c}{l_1-2c}\right] \end{aligned} \quad . \tag{27}$$

Similarly, the deflection curve of a transverse bar under compression was taken in the form of a Fourier sine series, expressed as

$$x = \sum_{i=1}^{\infty} b_{\text{II}i} \sin \frac{2i\pi y}{(l_2 - 2b)} \quad . \tag{28}$$

The strain energy of bending of a transverse bar was obtained as

$$\Delta U_{\mathrm{IIH1}} = \frac{EI}{2}\left[\int_0^{l_2-2b}\left(\frac{d^2x}{dy^2}\right)^2 dy + 2\int_{-b}^{0}\left(\frac{d^2x}{dy^2}\right)^2 dy\right]$$
$$= \frac{\pi^4 EI}{4\left(l_2-2b\right)^3}\sum_{i=1}^{\infty} i^4 b_{\mathrm{II}i}^2 + \frac{\pi^3 EI}{\left(l_2-2b\right)^3}\sum_{i=1}^{\infty}\left[\frac{i\pi b}{2\left(l_2-2b\right)} - \frac{1}{4}\sin\frac{2i\pi b}{l_2-2b}\right] i^3 b_{\mathrm{II}i}^2 \quad . \qquad (29)$$
$$- \frac{\pi^3 EI}{\left(l_2-2b\right)^3}\sum_{\substack{n,m=1\\ n\neq m}}^{\infty} n^2 m^2 b_{\mathrm{II}n} b_{\mathrm{II}m}\left[\frac{1}{n+m}\sin\frac{\left(n+m\right)\pi b}{l_2-2b} - \frac{1}{n-m}\sin\frac{\left(n-m\right)\pi b}{l_2-2b}\right]$$

The energy of deformation of elastic supports of a transverse bar was

$$\Delta U_{\mathrm{IIH2}} = \frac{\beta}{2}\left(\int_0^{l_2-2b} x^2 dy + 2\int_{-b}^{0} x^2 dy\right)$$
$$= \frac{\left(l_2-2b\right)\beta}{4}\sum_{i=1}^{\infty} b_{\mathrm{II}i}^2 + \frac{\left(l_2-2b\right)\beta}{\pi}\sum_{i=1}^{\infty}\left[\frac{i\pi b}{2\left(l_2-2b\right)} - \frac{1}{4}\sin\frac{2i\pi b}{l_2-2b}\right]\frac{1}{i} b_{\mathrm{II}i}^2 \quad . \qquad (30)$$
$$- \frac{\left(l_2-2b\right)\beta}{\pi}\sum_{\substack{n,m=1\\ n\neq m}}^{\infty} b_{\mathrm{II}n} b_{\mathrm{II}m}\left[\frac{1}{n+m}\sin\frac{\left(n+m\right)\pi b}{l_2-2b} - \frac{1}{n-m}\sin\frac{\left(n-m\right)\pi b}{l_2-2b}\right]$$

The displacement of a vertical bar from its initial straight form to the equilibrium curve under compression was

$$\lambda_{\mathrm{II}} = \frac{\left(2\pi\right)^2}{4\left(l_1-2c\right)}\sum_{i=1}^{\infty} a_{\mathrm{II}i}^2 + \frac{2\pi}{\left(l_1-2c\right)}\sum_{i=1}^{\infty}\left[\frac{i\pi c}{\left(l_1-2c\right)} + \frac{1}{4}\sin\frac{4i\pi c}{l_1-2c}\right]\frac{1}{i} a_{\mathrm{II}i}^2$$
$$+ \frac{nm\pi}{\left(l_1-2c\right)}\sum_{\substack{n,m=1\\ n\neq m}}^{\infty} a_{\mathrm{II}n} a_{\mathrm{II}m}\left[\frac{1}{n+m}\sin\frac{2\left(n+m\right)\pi c}{l_1-2c} + \frac{1}{n-m}\sin\frac{2\left(n-m\right)\pi c}{l_1-2c}\right] . \qquad (31)$$

The work done by compressive forces was obtained as

$$\Delta T_{\mathrm{II}} = 4P_{\mathrm{II}}\lambda_{\mathrm{II}} \ , \qquad (32)$$

where P_{II} is the compressive force acting on a vertical bar in frame-II.

Hence, the general equation for calculating the critical stress of frame-II was

$$\Delta U_{\mathrm{II}} = 4\left(\Delta U_{\mathrm{IIV1}} + \Delta U_{\mathrm{IIV2}}\right) + 12\left(\Delta U_{\mathrm{IIH1}} + \Delta U_{\mathrm{IIH2}}\right) = \Delta T_{\mathrm{II}} \quad . \qquad (33)$$

Substituting Eqs. 26, 27, 29, 30, and 32 into Eq. 33 and taking all parameters $a_{\mathrm{II}i}$ and $b_{\mathrm{II}i}$ except $a_{\mathrm{II}1}$ and $b_{\mathrm{II}1}$, equal to zero, the critical load of a vertical bar was obtained as

$$P_{\mathrm{IIcr}}=\frac{4\left\{\left[\pi mA_1+\frac{1}{16}A_2\right]+\left[2A_1+\frac{A_2}{8\pi}\cdot\frac{1}{m}\right]\left[A_3-\frac{1}{4}\sin 4A_3\right]\right\}+12\left\{\left[\pi mB_1+\frac{1}{16}B_2\right]\frac{l_2^4}{l_1^4}+\left[\frac{1}{4}B_1+\frac{B_2}{4\pi}\cdot\frac{1}{m}\right]\left[\frac{1}{2}B_3-\frac{1}{4}\sin 2B_3\right]\frac{l_2^4}{l_1^4}\right\}}{1+\frac{2}{m}\left[\frac{1}{\pi}A_3+\frac{1}{4\pi}\sin 4A_3\right]} \quad . \tag{34}$$

For given dimensions of bars and a given value of β, the following equation was used for determining m.

$$P_{\mathrm{IIcr}}(m)=P_{\mathrm{IIcr}}(m+1) \; . \tag{35}$$

Then, the critical load of the lattice frame-II was

$$P_{\text{frame-II}}=4P_{\mathrm{IIcr}} \quad . \tag{36}$$

(3) Lattice Frame-III

For frame-III (Fig.9), there were two kinds of deflection curves for the vertical bar with two points hinged by transverse bars under compression. The deflection curves of vertical bars at the four corners can be taken in the same form as vertical bars in lattice frame-I. Hence, the strain energy of bending of a vertical bar at the corner $\Delta U_{\mathrm{IIIV1}}$ was equal to ΔU_{IV1} and the energy of deformation of elastic supports of a vertical bar at the corner $\Delta U_{\mathrm{IIIV2}}$ was equal to ΔU_{IV2}.

Because lattice frame-III was a symmetric structure with respect to the plane of y = (l_2-2b)/2, the deflection curve of the middle vertical bar was also symmetric under compression. The deflection curves of the middle vertical bars were taken in the same form as vertical bars in frame-II. Hence, the strain energy of bending of the middle vertical bar $\Delta U'_{\mathrm{IIIV1}}$ was equal to ΔU_{IIV1} and the energy of deformation of the elastic supports of the middle vertical bar $\Delta U'_{\mathrm{IIIV2}}$ was equal to ΔU_{IIV2}.

Because the deflection of the transverse bar was symmetrical about the middle vertical bar under compression, the deflection curve of half of a transverse bar was taken in the form of a Fourier sine series, expressed as

$$x=\sum_{i=1}^{\infty} b_{\mathrm{III}i}\sin\frac{2i\pi y}{\left(l_2-2b\right)} \quad . \tag{37}$$

The strain energy of bending of a transverse bar was obtained as

$$\begin{aligned}\Delta U_{\mathrm{IIIH1}} &= \frac{EI}{2}\left[\int_0^{\frac{l_2-2b}{2}}\left(\frac{d^2x}{dy^2}\right)^2 dy+\int_{-b}^{0}\left(\frac{d^2x}{dy^2}\right)^2 dy\right]\times 2\\ &= \frac{4\pi^4 EI}{\left(l_2-2b\right)^3}\sum_{i=1}^{\infty} i^4 b_{\mathrm{III}i}^2+\frac{8\pi^3 EI}{\left(l_2-2b\right)^3}\sum_{i=1}^{\infty}\left[\frac{i\pi b}{\left(l_2-2b\right)}-\frac{1}{4}\sin\frac{4i\pi b}{l_2-2b}\right] i^3 b_{\mathrm{III}i}^2 \\ &\quad -\frac{8\pi^3 EI}{\left(l_2-2b\right)^3}\sum_{\substack{n,m=1\\ n\neq m}}^{\infty} n^2m^2 b_{\mathrm{III}n}b_{\mathrm{III}m}\left[\frac{1}{n+m}\sin\frac{2\left(n+m\right)\pi b}{l_2-2b}-\frac{1}{n-m}\sin\frac{2\left(n-m\right)\pi b}{l_2-2b}\right]\end{aligned} \quad . \tag{38}$$

The energy of deformation of the elastic supports of a transverse bar was

$$\begin{aligned}\Delta U_{\mathrm{IIIH2}} &= \left[\frac{\beta}{2}\left(\int_0^{\frac{l_2-2b}{2}} x^2dy+\int_{-b}^{0} x^2dy\right)\right]\times 2\\ &= \frac{\left(l_2-2b\right)\beta}{4}\sum_{i=1}^{\infty} b_{\mathrm{III}i}^2+\frac{\left(l_2-2b\right)\beta}{\pi}\sum_{i=1}^{\infty}\left[\frac{i\pi b}{\left(l_2-2b\right)}-\frac{1}{4}\sin\frac{4i\pi b}{l_2-2b}\right]\frac{1}{i} b_{\mathrm{III}i}^2 \\ &\quad -\frac{\left(l_2-2b\right)\beta}{2\pi}\sum_{\substack{n,m=1\\ n\neq m}}^{\infty} b_{\mathrm{III}n}b_{\mathrm{III}m}\left[\frac{1}{n+m}\sin\frac{2\left(n+m\right)\pi b}{l_2-2b}-\frac{1}{n-m}\sin\frac{2\left(n-m\right)\pi b}{l_2-2b}\right]\end{aligned} \quad . \tag{39}$$

Displacements of the vertical bar at corner and middle vertical bars from their initial straight forms to the equilibrium curves under compression were

$$\begin{aligned}\lambda_1 &= \frac{\pi^2}{4\left(l_1-2c\right)}\sum_{i=1}^{\infty} a_{\mathrm{III}i}^2+\frac{\pi}{\left(l_1-2c\right)}\sum_{i=1}^{\infty}\left[\frac{i\pi c}{2\left(l_1-2c\right)}+\frac{1}{4}\sin\frac{2i\pi c}{l_1-2c}\right]\frac{1}{i} a_{\mathrm{III}i}^2\\ &\quad +\frac{nm\pi}{2\left(l_1-2c\right)}\sum_{\substack{n,m=1\\ n\neq m}}^{\infty} a_{\mathrm{III}n}a_{\mathrm{III}m}\left[\frac{1}{n+m}\sin\frac{\left(n+m\right)\pi c}{l_1-2c}+\frac{1}{n-m}\sin\frac{\left(n-m\right)\pi c}{l_1-2c}\right]\end{aligned} \quad \text{and} \tag{40}$$

$$\begin{aligned}\lambda_2 &= \frac{\left(2\pi\right)^2}{4\left(l_1-2c\right)}\sum_{i=1}^{\infty} a_{\mathrm{III}i}^2+\frac{2\pi}{\left(l_1-2c\right)}\sum_{i=1}^{\infty}\left[\frac{i\pi c}{\left(l_1-2c\right)}+\frac{1}{4}\sin\frac{4i\pi c}{l_1-2c}\right]\frac{1}{i} a_{\mathrm{III}i}^2\\ &\quad +\frac{nm\pi}{\left(l_1-2c\right)}\sum_{\substack{n,m=1\\ n\neq m}}^{\infty} a_{\mathrm{III}n}a_{\mathrm{III}m}\left[\frac{1}{n+m}\sin\frac{2\left(n+m\right)\pi c}{l_1-2c}+\frac{1}{n-m}\sin\frac{2\left(n-m\right)\pi c}{l_1-2c}\right]\end{aligned} \quad . \tag{41}$$

Work done by compressive forces was obtained as

$$\Delta T_{\mathrm{III}} = 4P_{\mathrm{III}}\lambda_1 + 5P_{\mathrm{III}}\lambda_2 \quad . \tag{42}$$

Hence, the general equation for calculating the critical stress of frame-III was

$$\Delta U_{\mathrm{III}} = 4\left(\Delta U_{\mathrm{IIIV1}} + \Delta U_{\mathrm{IIIV2}}\right) + 5\left(\Delta U'_{\mathrm{IIIV1}} + \Delta U'_{\mathrm{IIIV2}}\right) + 12\left(\Delta U_{\mathrm{IIIH1}} + \Delta U_{\mathrm{IIIH2}}\right) = \Delta T_{\mathrm{III}} \quad . \tag{43}$$

Substituting Eqs. 1, 2, 15, 16, 27, 28, and 31 into Eq. 32 and setting all coefficients a_{IIIi} and b_{IIIi} except a_{III1} and b_{III1}, equal to zero, the critical load of a vertical bar was obtained as

$$P_{\mathrm{IIIcr}} = \frac{\begin{array}{l} 4\left\{\left[\frac{\pi m}{4}A_1 + \frac{1}{4}A_2\right] + \left[A_1 + \frac{A_2}{\pi}\cdot\frac{1}{m}\right]\left[\frac{1}{2}A_3 - \frac{1}{4}\sin 2A_3\right]\right\} \\ +5\left\{\left[4\pi m A_1 + \frac{1}{4}A_2\right] + \left[8A_1 + \frac{A_2}{2\pi}\cdot\frac{1}{m}\right]\left[A_3 - \frac{1}{4}\sin 4A_3\right]\right\} \\ +12\left\{\left[\pi m B_1 + \frac{1}{4}B_2\right]\frac{l_2^4}{l_1^4} + \left[8B_1 + \frac{B_2}{\pi}\cdot\frac{1}{m}\right]\left[B_3 - \frac{1}{4}\sin 4B_3\right]\frac{l_2^4}{l_1^4}\right\} \end{array}}{\left\{1 + \frac{4}{\pi m}\left[\frac{1}{2}A_3 + \frac{1}{4}\sin 2A_3\right]\right\} + \left\{5 + \frac{10}{\pi m}\left[A_3 + \frac{1}{4}4\sin A_3\right]\right\}} \quad . \tag{44}$$

For the given dimensions of bars and a given value of β, m was determined using

$$P_{\mathrm{IIIcr}}(m) = P_{\mathrm{IIIcr}}(m{+}1) \; . \tag{45}$$

Then, the critical load of lattice frame-III was

$$P_{\text{frame-III}} = 9P_{\mathrm{IIIcr}} \quad . \tag{46}$$

4.4 Ultimate axial load capacity

The ultimate axial load capacities of syntactic foam columns without a GFRP shell and syntactic foam filled-GFRP tubes was calculated using

$$P_{u1} = f_c^{'}A_c + P_{frame} \quad \text{and} \tag{47}$$

$$P_{u2} = f_c^{'}A_c + f_{cr}A_F + P_{frame} \quad , \tag{48}$$

where A_c and A_F are the cross-sectional areas of foam core and GFRP tube, respectively.

Comparisons of calculated and experimental results showed that the predicted results from the analytical model were in good agreement with experimental results (Table 3). The axial load capacity of foam-filled GFRP tubes was almost 2-fold higher than those of specimens without GFRP shells. The predicted axial load capacity of specimens with lattice frame reinforcement was increased by ~22%, compared with specimens without lattice frames. Decreasing the distances between GFRP bars in transverse or vertical directions resulted in a small increase in local buckling loads for specimens with and without GFRP shells. Specimens with lattice frame reinforcement had a similar local buckling performance as specimens reinforced with MWCNTs.

5 Conclusions

The structural response and energy absorption of syntactic foam composite columns under axial compression were investigated. The foam core was reinforced by a GFRP lattice frame and the reinforcement effects compared with those of MWCNTs. The results obtained from this study were summarized below:

(1) Lattice frame reinforcement in syntactic foam columns contributed to retard the separation of fragments from the foam. Syntactic foam-filled GFRP tubular columns without frames failed, with longitudinal splitting and delamination of GFRP shells accompanied by crushed fragments of foam core. In contrast, syntactic foam-filled GFRP tubular columns with frames exhibited progressive failures with lateral cracks of GFRP jackets and foam core extrusion. MWCNTs added to the foam did not change the failure modes of both bare syntactic foam and syntactic foam-filled GFRP tubular

columns.

(2) For syntactic foam columns without GFRP shells, the lattice frame contributed to increased energy absorption much more than to peak crushing load and axial stiffness. Varying the distance between the vertical or transverse bars had insignificant effects on the mechanical properties of syntactic foam columns without GFRP shells. Added MWCNT generated higher axial stiffness of syntactic foam columns than did lattice frame reinforcement, while the energy absorption of MWCNT-reinforced syntactic foam columns was a little lower than that of specimens with frame reinforcement.

(3) The compressive strength of syntactic foam-filled GFRP tubes with lattice frame reinforcement were significantly improved, especially regarding plateau stress, while stiffness increased insignificantly. Compared to counterparts without reinforcement, the energy absorption of specimens with GFRP shells and reinforcement increased by ~90% and their CFE ratios ~1 in the first post-yield phase. With decreased distances between transverse or vertical bars, the energy absorption of specimens with GFRP shells was increased. Moreover, the energy absorption ability of syntactic foam-filled GFRP tubular columns with reinforcement was much higher than that of counterparts reinforced by MWCNTs.

(4) An analytical model, considering the local buckling of lattice frames, was proposed based on an energy method to predict the ultimate axial compressive load, in which the action of the foam on vertical and transverse bars was replaced by equally spaced elastic supports with equal rigidity. This analytical model showed the capability to accurately predict the ultimate crushing loads of syntactic foam-filled GFRP tubular columns with

lattice frame reinforcement.

Acknowledgments

The financial support from the National Natural Science Foundation of China (Grant 51578283) and the Science and Technology Project of Jiangsu Construction System, China (Grant 2021ZD05).

References

[1] Ding LN, Liu X, Wang X, Huang HJ, Wu ZS. Mechanical properties of pultruded basalt fiber-reinforced polymer tube under axial tension and compression. Construction and Building Materials 2020; 176:629-637.

[2] Teng BG, Hu L, Yuan SJ. Deformation behavior of thin-walled tubes bending with internal pressure. Reviews on Advanced Materials Science 2013; 33(5):436-441.

[3] Yang H, Lei H, Lu G. Crashworthiness of circular fiber reinforced plastic tubes filled with composite skeletons/aluminum foam under drop-weight impact loading. Thin-Walled Structures 2021; 160:107380.

[4] Bao F, Wang J, Wang J, Zeng S, Guo X. Static and impact responses of syntactic foam composites reinforced by multi-walled carbon nanotubes. Journal of Materials Research and Technology 2020; 9(6):12391-12403.

[5] Bharath HS, Dileep B, Suhasini G, Pavana P, Mrityunjay D. Flexural response of 3D printed sandwich composite. Composite Structures 2021; 263:113732.

[6] Gupta N, Ye R, Porfiri M. Comparison of tensile and compressive characteristics of vinyl

ester/glass microballoon syntactic foams. Composites Part B 2009; 41(3):236-245.

[7] Ghosh D, Wiest A, Conner RD. Uniaxial quasistatic and dynamic compressive response of foams made from hollow glass microspheres. Journal of the European Ceramic Society 2016; 36:781-789.

[8] Tomlinson D, Fam A. Axial response of flax fibre reinforced polymer-skinned tubes with lightweight foam cores and bioresin blend. Thin-Walled Structures 2020; 155:106923.

[9] Wang L, Liu W, Fang Y, Wan L, Huo R. Axial crush behavior and energy absorption capability of foam-filled GFRP tubes manufactured through vacuum assisted resin infusion process. Thin-Walled Structures 2016; 98:263-273.

[10] Ghazijahani TG, Jian H, Holloway D. Timber filled CFRP jacketed circular steel tubes under axial compression. Construction and Building Materials 2015; 94:791-799.

[11] Hussein RD, Ruan D, Lu G, Sbarski I. Axial crushing behaviour of honeycomb-filled square carbon fibre reinforced plastic (CFRP) tubes. Composite Structures 2016; 140:166-179.

[12] Baroutaji A, Sajjia M, Olabi AG. On the crashworthiness performance of thin-walled energy absorbers: Recent advances and future developments. Thin-Walled Structures 2017; 118:137-163.

[13] Gao G, Hu Y, Jia H, Liu P, Du P, Xu D. Acoustic and dielectric properties of epoxy resin/hollow glass microsphere composite acoustic materials. Journal of Physics and Chemistry of Solids 2019; 135:109105.

[14] Zhang Z, Sun W, Zhao Y, Hou S. Crashworthiness of different composite tubes by experiments and simulations. Composites Part B: Engineering 2018; 143:86-95.

[15] Chen L, Pan D, Zhao Q, Chen L, Niu L, Cong L, Li C. Overall buckling characteristics of slender FRP-foam sandwich tube under axial compression. Composites Communications 2021; 24:100585.

[16] Sun G, Li S, Liu Q, Li G, Li Q. Experimental study on crashworthiness of empty/aluminum foam/honeycomb-filled CFRP tubes. Composite Structures 2016; 152:969-993.

[17] Fu K, Zhao Z, Jin L. Programmable granular metamaterials for reusable energy absorption. Advanced Functional Materials 2019; 29:1901258.

[18] Yu S, Li X, Zou M, Guo X, Ma H, Wang S. Effect of the Aromatic Amine Curing Agent Structure on Properties of Epoxy Resin-Based Syntactic Foams. ACS Omega 2020; 5(36):23268-23275.

[19] Li R, Wang P, Zhang P, Fan G, Wang G, Ouyang X, Ma N, Wei H. Surface modification of hollow glass microsphere and its marine-adaptive composites with epoxy resin. Advanced Composites Letters 2020; 29:1-8.

[20] Wang P, Zhong S, Yan K, Liao B, Zhang J. Influence of a batch of hollow glass microspheres with different strength grades on the compression strength of syntactic foam. Composites Science and Technology 2022; 223:109442.

[21] Huang R, Li P, Liu T. X-ray microtomography and finite element modelling of compressive failure mechanism in cenosphere epoxy syntactic foams. Composite Structures 2016; 140:157-165.

[22] Rousseau CE, Plume G, Goni M, Ale B. Behavior of syntactic foam under plate impact. Mechanics Research Communications 2017; 83:1-5.

[23] Swetha C, Kumar R. Quasi-static uni-axial compression behaviour of hollow glass microspheres/epoxy based syntactic foams. Materials and Design 2011; 32:4152-4163.

[24] Huang R, Li P. Elastic behaviour and failure mechanism in epoxy syntactic foams: The effect of glass microballoon volume fractions. Composites Part B 2015; 78:401-408.

[25] Gupta N, Woldesenbet E. Microballoon wall thickness effects on properties of syntactic foams.

Journal of Cellular Plastics 2004; 40:461-480.

[26] Ambika Devi K, John B, Reghunadhan Nair CP, Ninan KN. Syntactic foam composites of epoxy-allyl phenol-bismaleimide ternary blend-processing and properties. Journal of Applied Polymer Science 2008; 105(6):3715-3722.

[27] Qi C, Yu Q, Zhao Y. Fabrication and characterization of the thermoplastic and thermoset syntactic foam core-based sandwich composites. Polymer Composites 2020; 41(8):3052-3061.

[28] Omar YM, Xiang C, Gupta N, Strbik OM, Cho K. Syntactic foam core metal matrix sandwich composite: Compressive properties and strain rate effects. Materials Science & Engineering A 2015; 643:156-168.

[29] Breunig P, Damodaran V, Shahapurkar K, Waddar S, Doddamani M, Jeyaraj P, Prabhakar P. Dynamic impact behavior of syntactic foam core sandwich composites. Journal of Composite Materials 2020; 54(4):535-547.

[30] Ahmadi E, Atrian A, Fesharaki JJ, Montazerolghaem H, Saberi S. Experimental and numerical assessment of high-velocity impact behavior of syntactic foam core sandwich structures. European Journal of Mechanics/A Solids 2021; 90:104355.

[31] Li G, Muthyala VD. Impact characterization of sandwich structures with an integrated orthogrid stiffened syntactic foam core. Composites Science and Technology 2008; 68:2078-2084.

[32] Wang J, GangaRao H, Li M, Liang R, Liu W. Axial behavior of columns with glass fiber-reinforced polymer composite shells and syntactic foam core. Journal of Composites for Construction 2019; 23(2):04018083.

[33] Kumar SJA, Ahmed KS. Compression behavior and energy absorption capacity of stiffened syntactic foam core sandwich composites. Journal of Reinforced Plastics and Composites 2013;

32(18):1370-1379.

[34] Huang W, Xu H, Fan Z, Jiang W, Liu J. Dynamic failure of ceramic particle reinforced foam-filled composite lattice core. Composites Science and Technology 2020; 193:108143.

[35] Alia RA, Cantwell WJ, Langdon GS, Yuen SCK, Nurick GN. The energy-absorbing characteristics of composite tube-reinforced foam structures. Composites Part B 2014; 61:127-135.

[36] An X, Fan H. Hybrid design and energy absorption of luffa-sponge-like hierarchical cellular structures. Materials & Design 2016; 106:247-257.

[37] Zhou J, Guan Z, Cantwell WJ. The energy-absorbing behaviour of composite tube-reinforced foams. Composites Part B 2018; 139:227-237.

[38] Zhang Y, Yan X, Huang W, Lin J. Experimental investigations on mechanical behavior of the carbon fiber tube reinforced polyurethane foam. Thin-Walled Structures 2020; 155:106899.

[39] Esmaeili A, Ma D, Manes A, Oggioni T, Jiménez-Suárez A, Ureña A, Hamouda AMS, Sbarufatti C. An experimental and numerical investigation of highly strong and tough epoxy based nanocomposite by addition of MWCNTs: Tensile and mode I fracture tests. Composite Structures 2020; 252:112692.

[40] Wang Y, Wang J, Wang J, Hui D. Experimental and multiscale numerical investigations on low-velocity impact responses of syntactic foam composites reinforced with modified MWCNTs. Nanotechnology Reviews 2021; 10:883-903.

[41] Khashaba UA. Toughness, flexural, damping and interfacial properties of hybridized GFRE composites with MWCNTs. Composites Part A 2015; 68:164-176.

[42] Qiao Y, Li Q, Li Q, Bian X, Lu C, Yang K, Zheng T, Zhang X, Wang X. Lightweight epoxy foams prepared with arranged hollow-glass-microspheres/epoxy hollow spheres. Composites

Communications 2022; 33:101197.

[43] Wang P, Zhong S, Yan K, Liao B, Zhang J. Influence of a batch of hollow glass microspheres with different strength grades on the compression strength of syntactic foam. Composites Science and Technology 2022; 223:109442.

[44] Liu Q, Shen H, Wu Y, Xia Z, Fang J, Li Q. Crash responses under multiple impacts and residual properties of CFRP and aluminum tubes. Composite Structures 2018; 183:416-422.

[45] Othman A, Abdullah S, Ariffin AK, Mohamed NAN. Investigating the quasi-static axial crushing behavior of polymeric foam-filled composite pultrusion square tubes. Materials and Design 2014; 63:446-459.

[46] Maranan GB, Manalo AC, Benmokrane B, Karunasena W, Mendis P. Behavior of concentrically loaded geopolymer-concrete circular columns reinforced longitudinally and transversely with GFRP bars. Engineering Structures 2016; 117:422-436.

[47] Paultre P, Légeron F. Confinement reinforcement design for reinforced concrete columns. Journal of Structural Engineering 2008; 134:738-749.

[48] Lam L, Teng JG. Design-oriented stress-strain model for FRP-confined concrete. Construction and Building Materials 2003; 17(6):471-489.

[49] Timoshenko SP, Gere JM. Theory of elastic stability, 2nd ed. McGraw-Hill, New York. 1961.

[50] Vinson JR, Sierakowski RV. The behavior of structures composed of composite materials, 2nd ed. Springer, Netherlands. 2008.

Table 1 Properties of syntactic foam composites

Property	Syntactic foam	Syntactic foam with 0.6-wt% MWCNTs	Syntactic foam with 1.2-wt% MWCNTs
Compressive strength (MPa)/δ (%)	18.23/4.65	20.56/4.76	21.86/2.34
Compressive modulus (GPa)/δ (%)	0.60/4.43	0.62/3.78	0.69/3.46
Tensile strength (MPa)/δ (%)	7.32/5.54	8.87/3.25	9.04/4.56
Young's modulus (GPa)/δ (%)	0.62/4.65	0.64/3.67	0.71/4.25
Density (kg/m^3)	424	432	434

Table 2 Experimental results

Specimens	P_{max} (kN)	$P_m/P_{m1}/P_{m2}$ (kN)	K (kN/mm)	m (g)	E (J)	SEA (J/g)	$CFE/CFE_1/CFE_2$
S70	33.52	11.40/-/-	11.09	66.51	925.59	13.92	0.34/-/-
S70-I	40.26	22.15/-/-	11.24	67.53	1299.10	19.24	0.55/-/-
S70-II	41.72	17.80/-/-	11.80	68.06	1238.61	18.20	0.43/-/-
S70-III	39.30	21.08/-/-	12.26	68.52	1261.80	18.42	0.54/-/-
S70C0.6	37.09	16.87/-/-	11.64	67.82	1074.56	15.84	0.45/-/-
S70C1.2	39.39	17.95/-/-	13.41	68.14	1219.21	17.89	0.46/-/-
FS70	69.77	-/52.11/37.64	30.65	111.51	2624.89	23.54	-/0.75/0.54
FS70-I	91.47	-/90.14/76.26	32.65	112.52	4559.65	40.52	-/0.99/0.83
FS70-II	92.27	-/89.21/62.28	34.84	113.06	4554.84	40.29	-/0.97/0.67
FS70-III	93.05	-/96.18/48.24	36.31	113.59	5000.78	44.02	-/1.03/0.52
FS70C0.6	87.64	-/61.95/43.19	31.49	112.82	3033.44	26.89	-/0.71/0.49
FS70C1.2	92.39	-/75.96/33.73	45.85	113.14	3214.14	28.41	-/0.82/0.37

Notes: In the first column, the first letters S and F mean the syntactic foam columns without GFRP shell and syntactic foam-filled GFRP tubes, respectively, 70 means the syntactic foam containing 70-vol% HGMs, C0.6 and C1.2 mean the foam is reinforced by 0.6-wt% and 1.2-wt% MWCNTs, respectively, and I, II, and III mean the foam is reinforced by lattice frame-I, II and III, respectively.

Table 3 Comparison of theoretical and experimental results

Specimens	$P_{\max}$ (kN)	P_u (kN)	$\delta=\frac{P_u-P_{max}}{P_{max}}\times 100\%$
S70	33.52	35.19	4.98
S70-I	40.26	41.59	3.30
S70-II	41.72	42.97	3.00
S70-III	39.30	43.19	9.90
S70C0.6	37.09	38.63	4.15
S70C1.2	39.39	39.25	-0.36
FS70	69.77	77.04	10.42
FS70-I	91.47	91.88	0.45
FS70-II	92.27	93.36	1.18
FS70-III	93.05	94.06	1.09
FS70C0.6	87.64	90.42	3.17
FS70C1.2	92.39	96.29	4.22

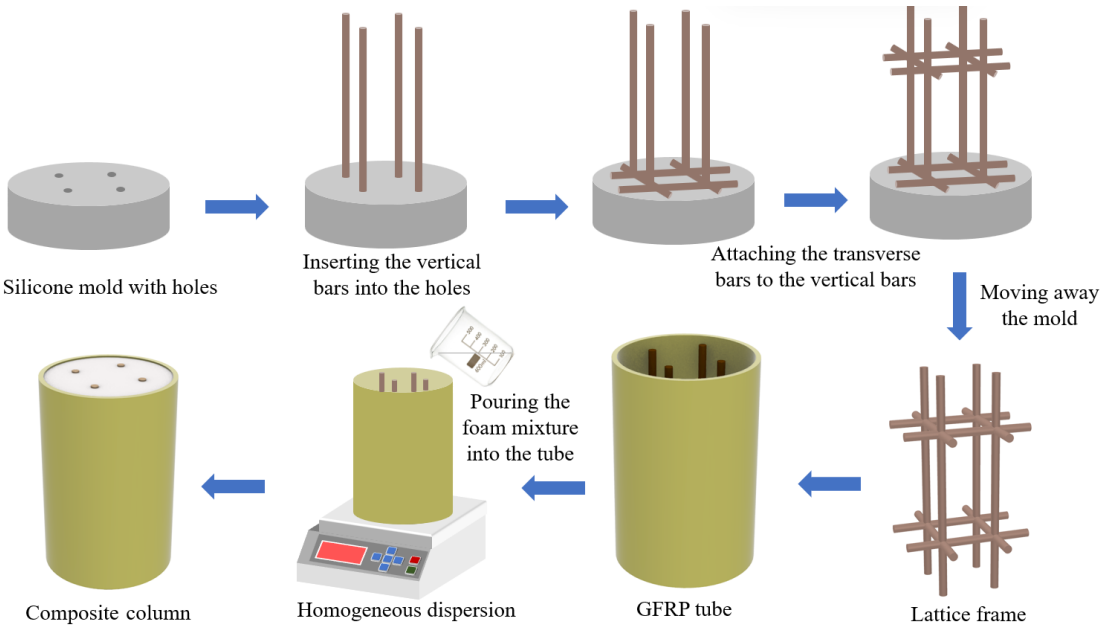

Fig. 1. Fabrication procedure of composite columns with lattice frame reinforcements

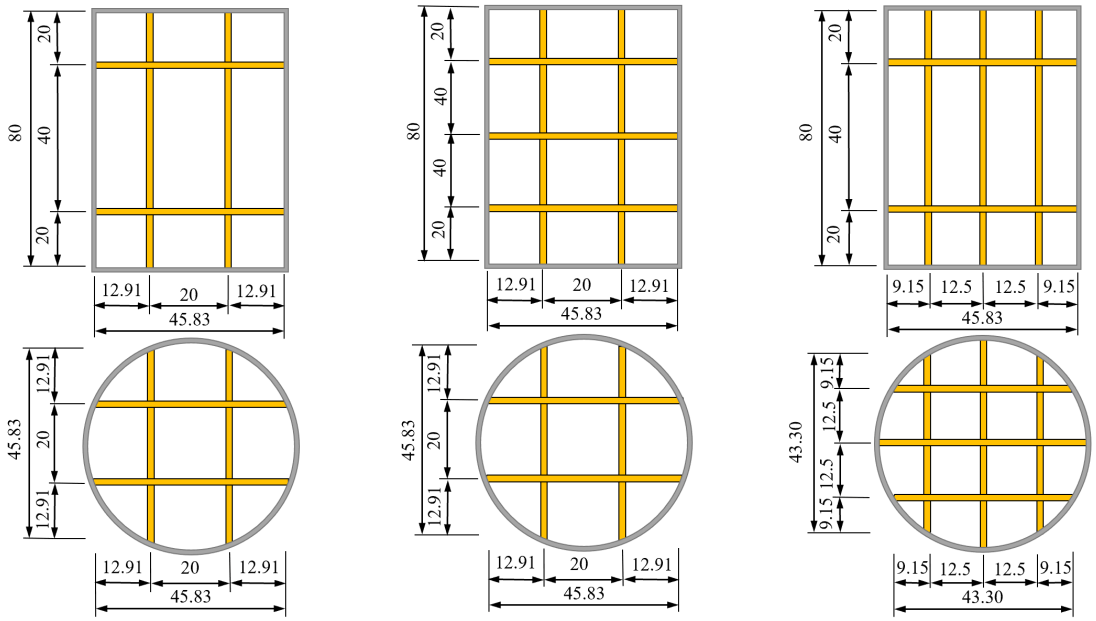

(a) Lattice frame-I (b) Lattice frame-II (c) Lattice frame-III

Fig. 2. Dimensions of syntactic foam-filled GFRP tubular columns with lattice frames (units: mm)

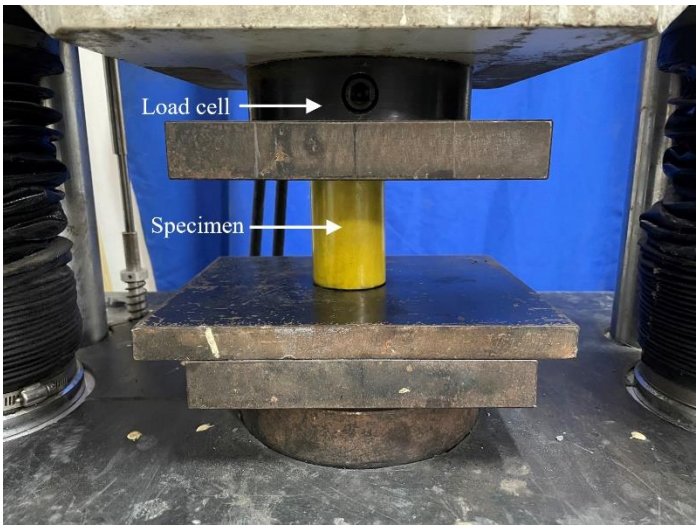

Fig. 3. Test set-up

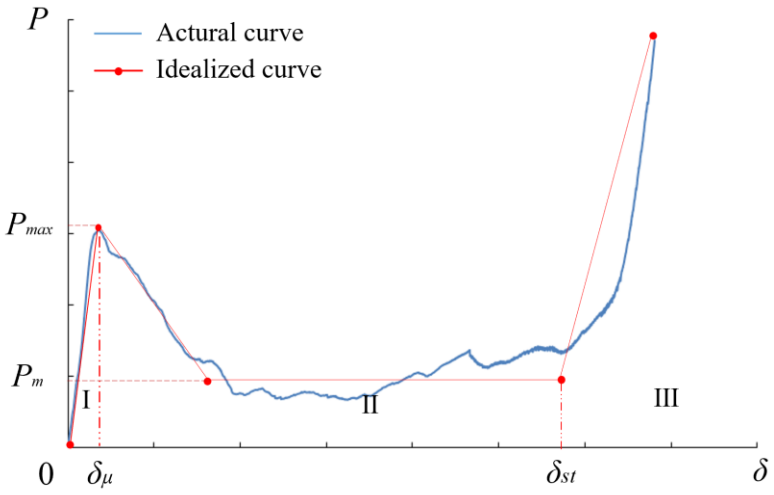

(a) Syntactic foam columns

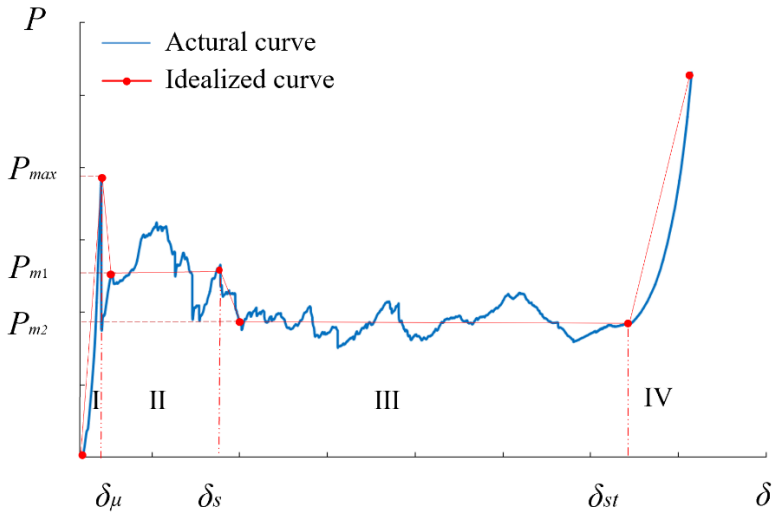

(b) Syntactic foam-filled GFRP tubular columns without lattice frame reinforcements

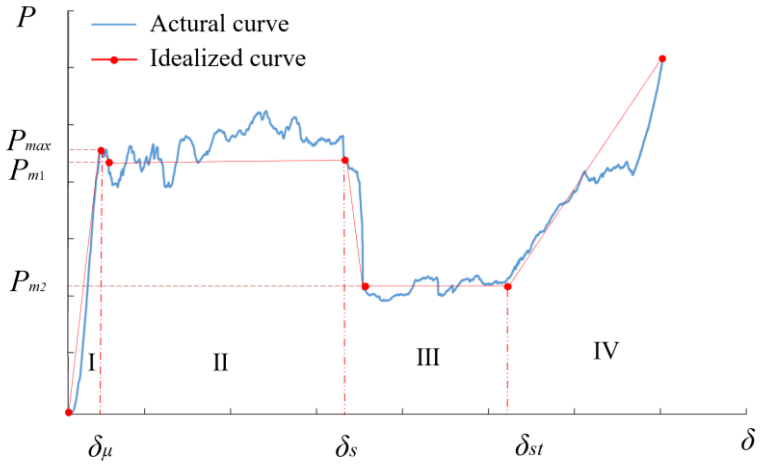

(c) Syntactic foam-filled GFRP tubular columns with lattice frame reinforcements

Fig. 4. Typical load-displacement curves

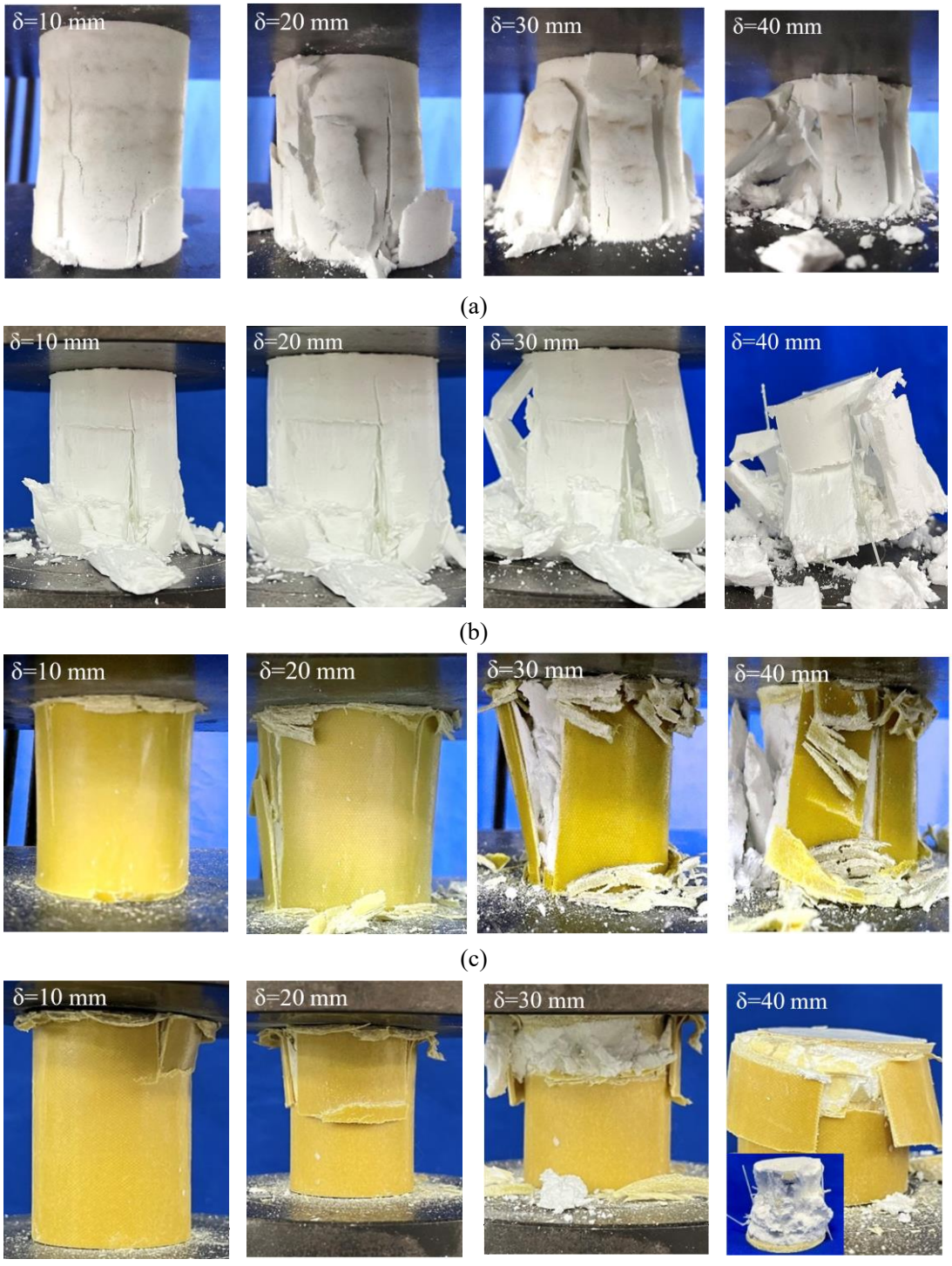

Fig. 5. Progressive failure of typical specimens: (a) bare syntactic foam columns (S70); (b) syntactic foam columns with lattice frame reinforcements (S70-III); (c) syntactic foam-filled GFRP tubular columns without lattice frame reinforcements (FS70); and (d) syntactic foam-filled GFRP tubular columns with lattice frame reinforcements (FS70-III)

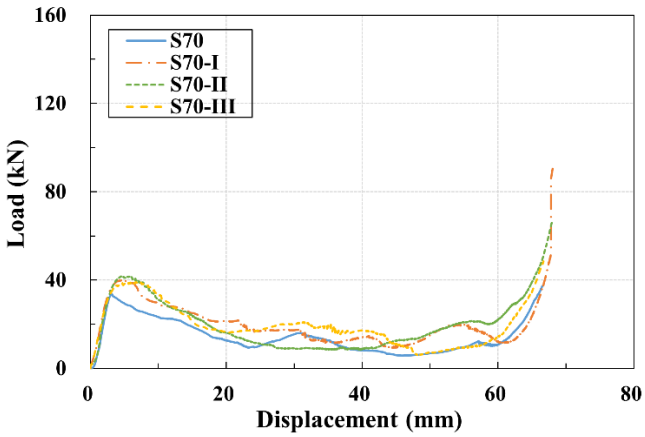

(a) Effect of the lattice frame for syntactic foam columns

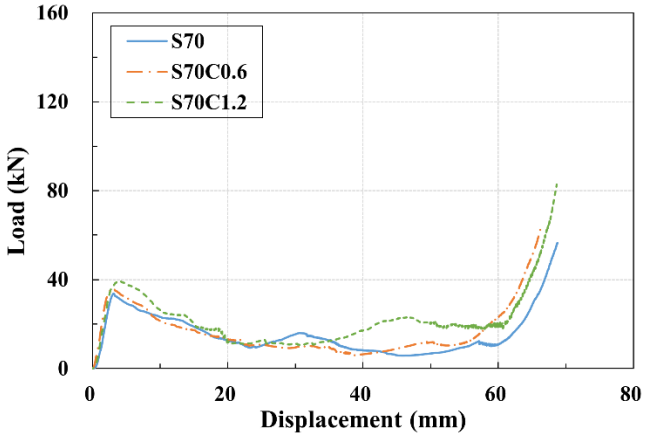

(b) Effect of MWCNTs for syntactic foam columns

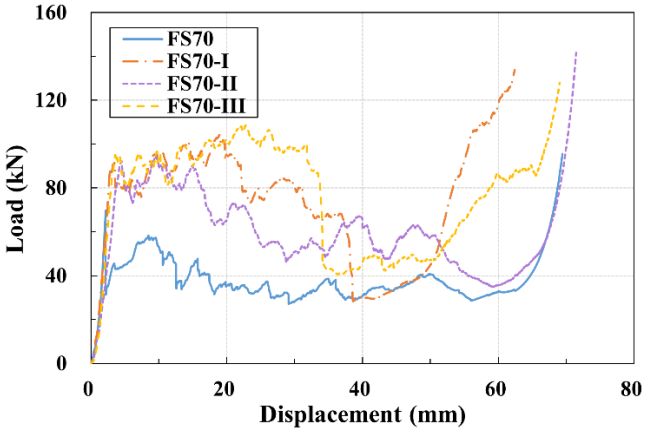

(c) Effect of the lattice frame for syntactic foam-filled GFRP tubes

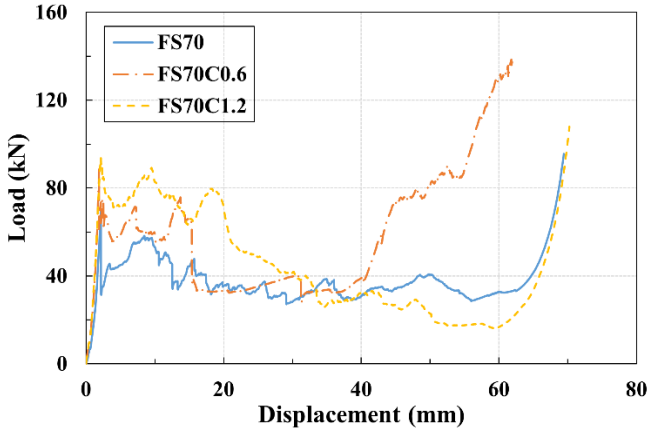

(d) Effect of MWCNTs for syntactic foam-filled GFRP tubes

Fig. 6. Load-displacement responses

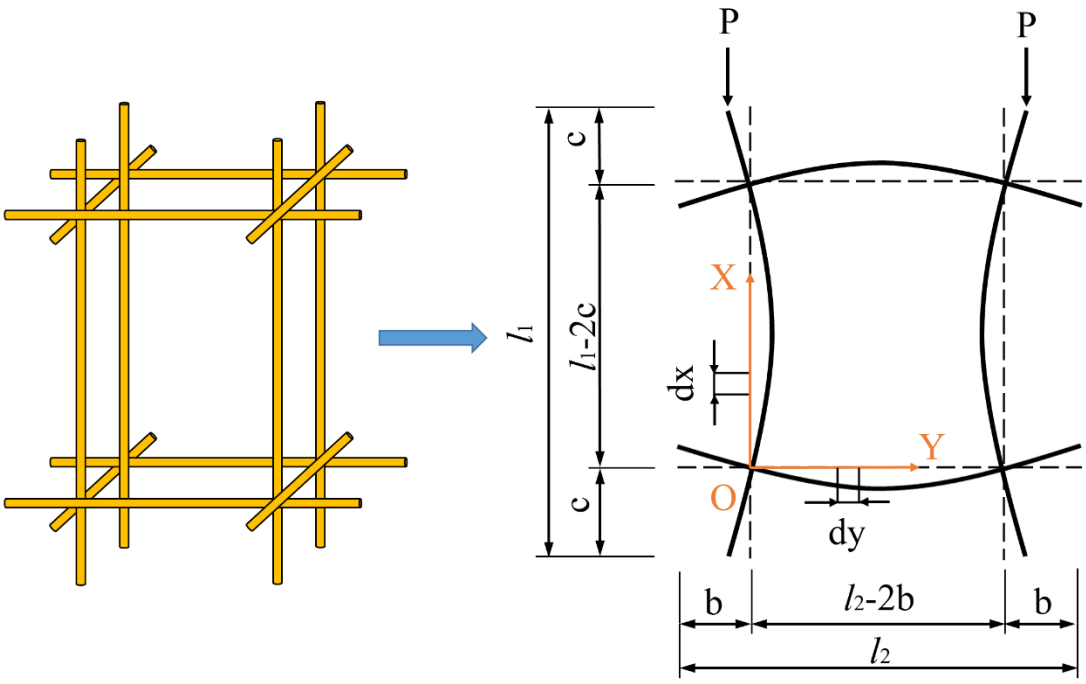

Fig. 7. Load diagram of lattice frame-I

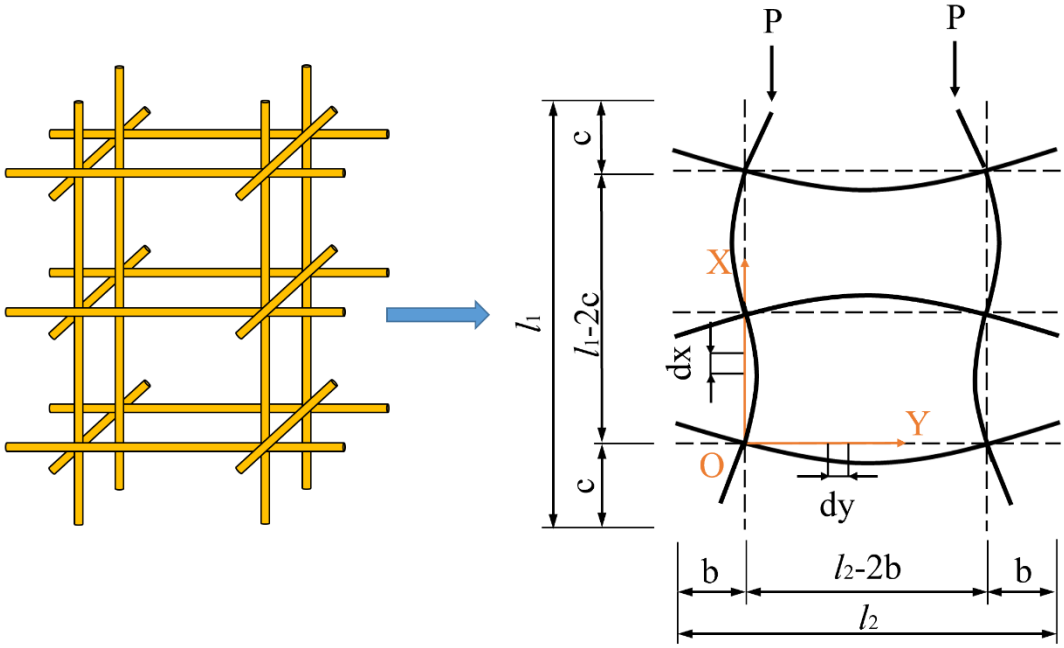

Fig. 8. Load diagram of lattice frame-II

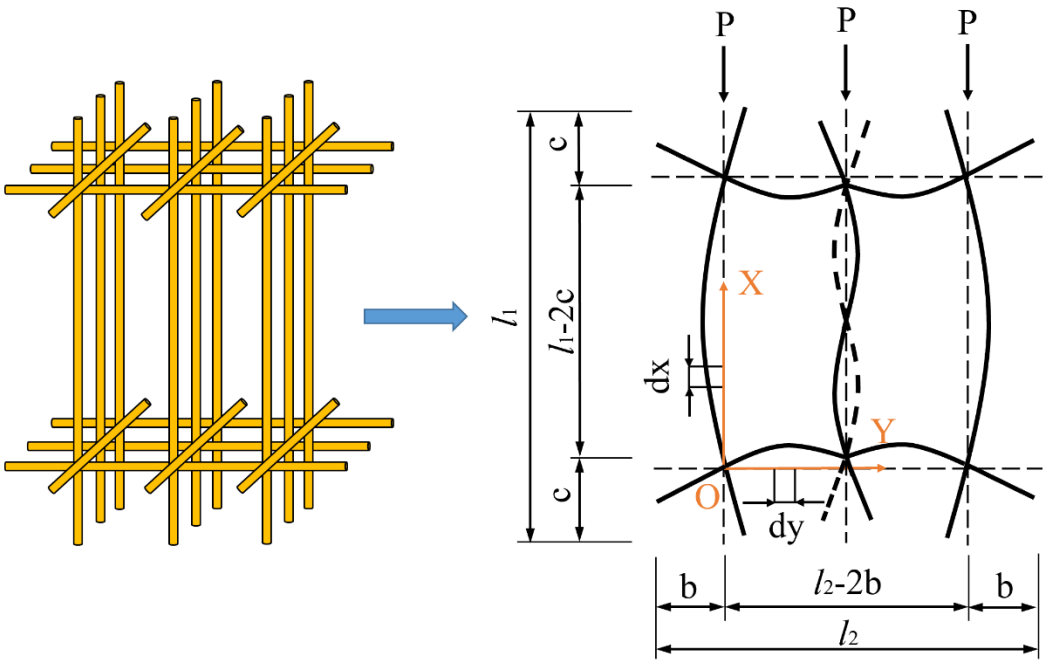

Fig. 9. Load diagram of lattice frame-III